Supporting Information

Hahm et al. 10.1073/pnas.1315667111

SI Methods

Bulk Geochemistry, Geology, and Tree-Canopy Cover. We collected bedrock using a sledgehammer or gas-powered drill to obtain the freshest (least-weathered) samples possible. Sample locations were determined by handheld Global Positioning System devices and are generally accurate to an estimated 20 m or less. In the laboratory, we crushed each sample and powdered a ∼40-g subsample to <50 microns in a tungsten carbide shatterbox. Powders were fired at 550 °C for 12 h to drive off water and organic material. For major- and minor-element geochemistry (reported in both wt % and mg/g in Dataset S3) we fused carefully massed powders and lithium tetraborate (typically at a ratio of 1:9) into beads in an autofluxer. For trace-element geochemistry (reported in ppm in Dataset S3) we pressed sample powder with SPEX Ultrabind binder into cylindrical pellets. The resulting beads and pellets were analyzed by X-ray flourescence (XRF) using a 4000-W wavelength-dispersive XRF spectrometer at the University of Wyoming (UW). Major-, minor-, and trace-element data are reported in Dataset S3. Major rock-forming elements are shown in Figs. 2 and 3 and Fig. S3. Element concentrations shown in Fig. S4 were reported in ref. 1. Accuracy of the UW XRF spectrometer was usually ±1% of the measured concentration for high-abundance major elements, but was somewhat poorer (e.g., ±3%) for low-abundance minor elements. Trace-element data were generally reproducible to within 10% in duplicate pellets for elements reported in Datasets S3 and S4.

We grouped samples into sites first by rock type (and hence geochemistry and mineralogy) and second by proximity. We classified rocks based on observed mineralogy or geochemistry and by intersection of sample locations with digitized geologic maps (2). To match sample locations with climate, topography, and vegetation, we intersected sample locations with available datasets of elevation, mean annual precipitation (3), mean annual temperature (3), and remotely sensed tree-canopy cover (4). The native resolution of the tree-canopy cover dataset is 30 m, but we resampled the raster so that each pixel took on the average value of the pixels within a ∼150-m radius of each sample point. Our measurements of bedrock geochemistry and field observations of mineralogy indicate that bulk geochemistry is generally uniform over this scale within individual plutons. Varying the size of the averaging window for tree-canopy cover does not significantly alter any of the trends shown in Figs. 2 and 3.

Biomass Survey and Tree Cores for Primary Productivity. For two of the rock types shown in Fig. 2, we delineated plots around forest stands that are representative of our bedrock sample sites (at the stars shown in Fig. 2). We measured the diameters of all trees with diameter at breast height (DBH) > 10 cm and estimated aboveground stem biomass using species-specific allometric equations found in the Software for Computing Plant Biomass (BIOPAK) library (5). We randomly selected and cored a subset of trees that were representative in size of the trees at each plot. We counted annual tree growth rings from the cores to estimate the age of each tree and then estimated lifetime-integrated growth rates (i.e., productivity) for each tree by dividing biomass by age. For each site, we extrapolated the mean lifetime-integrated productivity of the cored trees to the entire stand and thus estimated average plot-wide productivity per unit area (Datasets S1 and S2). The average productivity of the site developed on Bass Lake tonalite is 0.36 ± 0.11 kg m^{-2} y^{-1} stem biomass, which is 14.4 times higher than the estimated productivity of 0.025 ± 0.06 kg m^{-2} y^{-1} stem biomass at the Bald Mountain site. We judge that these estimates represent a realistic assessment of the relative differences in productivity among the sites. However, as absolute measures they may be inaccurate. Moreover there are potential biases to consider in any comparisons. For example, our data indicate that trees have grown faster as they have aged. This may introduce a bias due to differences in mean stand age between the plots. Trees on the tonalite plot are younger on average than on the granite plot. Together, the age-dependent growth rate and difference in age would make the measured differences in productivity between two rock types seem less pronounced than they actually are. Hence, based on known potential biases in our analysis, we judge that our estimate of the difference in productivity is conservative in representing Bald Mountain as a less productive site.

Erosion Rates from ^{10}Be. We measured ^{10}Be concentrations in quartz to assess rates of erosion from soil-mantled and exposed-bedrock terrain in the CZO vicinity. Our analysis includes both catchment-wide averages measured from stream sediment and point measurements from slopes. We separated quartz from our samples using standard techniques (6, 7) and then spiked the quartz with ^{9}Be, dissolved it, and extracted Be at UW following standard procedures. $^{10}Be/^{9}Be$ ratios were measured by accelerator mass spectrometry (AMS) at the Purdue Rare Isotope Measurement Laboratory (8) and calibrated with revised ICN Biomedical standards. Process blanks typically had $^{10}Be/^{9}Be$ ratios $<10 \times 10^{-15}$. We use the AMS data to calculate ^{10}Be concentrations in quartz. Results are reported in Dataset S6.

We determined site-specific rates of ^{10}Be production due to cosmic-ray muons and high-energy neutrons using relationships from Granger and Smith (9) and scaling factors for latitude and atmospheric pressure from Stone (10). Elevation, atmospheric pressure, and latitude were determined from 30-m DEMs. We corrected production rates for local shielding by biomass using a 30-m pixel resolution dataset (11). We also corrected for snow shielding (12) using a local relationship between snow–water equivalent and elevation constructed from snow-course data (13). We corrected for topographic and self-shielding of bedrock surfaces and catchments (14) using average slopes calculated from best-fit planar surfaces to catchment rims.

Using standard techniques (15–17) we inferred erosion rates from the ^{10}Be concentrations and production rates, correcting data from soil-mantled terrain for biases introduced by chemical erosion (18). Results are shown in Fig. 4 and compiled in Dataset S6. Reported uncertainties in erosion rates are propagated from analytical uncertainties of $^{10}Be/^{9}Be$ from the AMS measurements.

Landsat False-Color Images. Images shown in Figs. 1 and 2 were mosaicked from scenes taken in 2011 by the Landsat 5 Thematic Mapper. We use false color to highlight contrasts between vegetation and exposed bedrock; red is band 5 (reflected infrared with wavelength 1.55–1.75 μm), green is band 4 (reflected infrared with wavelength 0.76–0.90 μm), and blue is band 3 (red with wavelength 0.63–0.69 μm) (19).

Discussion

Lack of High-Intensity Fire and Anthropogenic Disturbance on Bare Areas. Although ecosystems in the Sierra Nevada have coevolved with fire (20), high-intensity burns can create spatial heterogeneities in forest cover (21). However, field evidence for fire, including burnt stumps and fire-induced spallation cracking (22), is scarce on prominent bare areas including Bald Mountain, Shuteye Peak, and Snow Corral Meadow. Therefore, we judge it unlikely that these areas have recently experienced fire of the magnitude needed to strip vegetation at the pluton scale. However, differences in available fuel across sites with differences in biomass likely affect the intensity of fires and play a role in the nature and timing of forest response to disturbance. Furthermore, postfire primary succession may be limited by both N availability and by P availability at sites with low parent-material P concentrations. We observe no evidence of cut stumps in the exposed-bedrock areas studied here. Hence there is no evidence that the dichotomy in forest cover is related to widespread anthropogenic disturbance.

Bedrock Fractures. Across our sites, bedrock fracturing is obscured by a mantle of soil, making it difficult to assess the role of fractures in the distribution of vegetation. In the Sierra Nevada, numerous mechanisms for fracture generation have been proposed (main text). However, no study has demonstrated a systematic connection between bedrock composition and fracturing. Such a connection would be expected if fracturing is an important regulator of vegetation; the strong correlations presented in Fig. 3 imply that anything that strongly influences vegetation should be correlated with bedrock composition as well. It is possible that fracture production varied in the course of pluton emplacement, which could produce correlations with bedrock composition. However, the relative and absolute emplacement history of the different plutons studied here offers insight on the potential for such correlations. In general, as the Sierra Nevada Batholith coalesced, bedrock composition typically graded from mafic to felsic with successive emplacement of different plutons (3). In theory, this could produce a correlation between composition and fracture density, if the processes of fracture production varied over time as plutons were emplaced. However, this is unlikely given that our sites span multiple, overprinted sequences of pluton emplacement. For example, the felsic Shuteye Peak granite was intruded by more mafic plutons at around 105 Ma (2, 23; Fig. 1*C*). In contrast, sometime after ∼100 Ma, the Dinkey Creek Granodiorite was intruded by the more felsic Bald Mountain Granite (23, 24; Fig. 1*D*). A complicated history of fracture production would be needed to produce a strong correlation between emplacement-related fracturing and geochemistry. This argues against strong fracture control of the vegetation trends shown in Fig. 3. However, we cannot rule it out in the absence of fracture density measurements across the sampling sites.

Erosion Rates from Cosmogenic Nuclides: Literature Compilation. We used a recent compilation of cosmogenic-nuclide–based erosion rates (25) as a starting point for the data-mining effort that resulted in Dataset S7, which is plotted in Fig. 4 (main text, gray symbols). Data are reported here as they originally appeared in the literature. We restricted our worldwide survey to nonglaciated sites underlain by granitic bedrock (16, 26–62). We compiled both ^{10}Be and ^{26}Al data from bedrock, saprolite, and detrital sediment. If separate erosion rates were reported from both ^{10}Be and ^{26}Al measurements, we include only the rate inferred from ^{10}Be. Where replicate analyses of the same sample were reported, we averaged the erosion rates inferred from each replicate and appended sample names with "_av" in Dataset S7. Averages were calculated using the inverse of reported erosion rates because the measured parameter (i.e., nuclide concentration) scales with the inverse of erosion rate (16).

1. Bateman PC, Dodge FCW, Bruggman PE (1984) *Major Oxide Analyses, CIPW Norms, Modes, and Bulk Specific Gravities of Plutonic Rocks from the Mariposa 1° X 2° Sheet, Central Sierra Nevada, California* (US Dept of the Interior, US Geol Surv, Washington, DC).
2. Bateman PC (1992) *Plutonism in the Central Part of the Sierra Nevada Batholith* (US. Govt Print Off, Washington, DC).
3. PRISM Climate Group (2013) Climate data. Available at www.prismclimate.org.
4. Homer C, et al. (2007) Completion of the 2001 National Land Cover Database for the conterminous United States. *Photogramm Eng Remote Sens* 73(4):1–5.
5. Means J, Hansen HA, Koerper GJ, Alaback P, Klopsch M (1994) *Software for Computing Plant Biomass—BIOPAK Users Guide* (US Dept of Agric, Washington, DC).
6. Kohl CP, Nishiizumi K (1992) Chemical isolation of quartz for measurement of in-situ-produced cosmogenic nuclides. *Geochim Cosmochim Acta* 56(9):3583–3587.
7. Purdue University Department of Physics (2013), Purdue Rare Isotope Measurement Laboratory. Available at www.physics.purdue.edu/primelab/. Accessed July 1, 2013.
8. Muzikar P, Elmore D, Granger DE (2003) Accelerator mass spectrometry in geologic research. *Geol Soc Am Bull* 115(6):643–654.
9. Granger DE, Smith AL (2000) Dating buried sediments using radioactive decay and muogenic production of Al-26 and Be-10. *Nucl Instrum Meth B* 172(1-4):822–826.
10. Stone JOH (2000) Air pressure and cosmogenic isotope production. *J Geophys Res* 105(B10):23753–23759.
11. Kellndorfer J, et al. (2012) *NACP Aboveground Biomass and Carbon Baseline Data (NBCD 2000), U.S.A., 2000* (ORNL DAAC) Available at http://dx.doi.org/10.3334/ORNLDAAC/1081.
12. Gosse JC, Phillips FM (2001) Terrestrial in situ cosmogenic nuclides: Theory and application. *Quat Sci Rev* 20(14):1475–1560.
13. California Department Water Resources (2013) California Data Exchange Center. Available at http://cdec.water.ca.gov.
14. Dunne JA, Elmore D, Muzikar P (1999) Scaling factors for the rates of production of cosmogenic nuclides for geometric shielding and attenuation at depth on sloped surfaces. *Geomorphology* 27(1-2):3–11.
15. Lal D (1991) Cosmic-ray labeling of erosion surfaces: In situ nuclide production rates and erosion models. *Earth Planet Sci Lett* 104(2-4):424–439.
16. Granger DE, Kirchner JW, Finkel RC (1996) Spatially averaged long-term erosion rates measured from in situ-produced cosmogenic nuclides in alluvial sediment. *J Geol* 104(3):249–257.
17. Granger DE, Riebe CS (2014) *Treatise on Geochemistry*, ed Drever JI (Elsevier, Oxford), 2nd Ed, pp 401–436.
18. Riebe CS, Granger DE (2013) Quantifying effects of deep and near-surface chemical erosion on cosmogenic nuclides in soils, saprolite, and sediment. *Earth Surf Process Landf* 38(5):523–533.
19. US Geological Survey (2012) *Landsat-A Global Land-Imaging Mission: U.S. Geological Survey Fact Sheet 2012–3072* (US Geol Surv, Sioux Falls, SD).
20. Swetnam TW (1993) Fire history and climate change in giant sequoia groves. *Science* 262(5135):885–889.
21. Miller C, Urban DL (1999) Interactions between forest heterogeneity and surface fire regimes in the southern Sierra Nevada. *Can J Res* 29(2):202–212.
22. Bierman PR, Gillespie AR (1991) Range fires: A significant factor in exposure-age determination and geomorphic surface evolution. *Geology* 19(6):641–673.
23. Lackey JS, et al. (2012) The Fine Gold Intrusive Suite: The roles of basement terranes and magma source development in the Early Cretaceous Sierra Nevada batholith. *Geosphere* 8(2):292–313.
24. Bateman PC, Wones DR (1972) *Geologic Map of the Huntington Lake Quadrangle, Central Sierra Nevada, California*. *US Geol Surv Geol Quad Map*. (US Geol Surv, Washington, DC).
25. Portenga EW, Bierman PR (2011) Understanding Earth's eroding surface with Be-10. *GSA Today* 21(8):4–10.
26. Bierman PR, Caffee MW (2001) Slow rates of rock surface erosion and sediment production across the Namib Desert and escarpment, southern Africa. *Am J Sci* 301(4-5):326–358.
27. Bierman PR, Caffee MW (2002) Cosmogenic exposure and erosion history of Australian bedrock landforms. *Geol Soc Am Bull* 114(7):787–803.
28. Bierman PR, et al. (2007) 10-Be shows that Namibian drainage basins are slowly, steadily, and uniformly eroding. *Quat Int* 167–168(3):33.
29. Binnie SA, Phillips WM, Summerfield MA, Fifield LK (2006) Sediment mixing rapidly and basin-wide cosmogenic nuclide analysis in eroding mountainous environments. *Quat Geochronol* 1(1):4–14.
30. Binnie SA, Phillips WM, Summerfield MA, Fifield LK (2007) Tectonic uplift, threshold hillslopes, and denudation rates in a developing mountain range. *Geology* 35(8):743–746.
31. Brown ET, Stallard RF, Larsen MC, Raisbeck GM, Yiou F (1995) Denudation rates determined from the accumulation of in situ-produced Be-10 in the Luquillo Experimental Forest, Puerto Rico. *Earth Planet Sci Lett* 129(1-4):193–202.
32. Brown ET, et al. (1998) Determination of predevelopment denudation rates of an agricultural watershed (Cayaguas River, Puerto Rico) using in-situ-produced Be-10 in river-borne quartz. *Earth Planet Sci Lett* 160(3-4):723–728.
33. Clapp EM, et al. (2000) Sediment yield exceeds sediment production in arid region drainage basins. *Geology* 28(11):995–998.
34. Clapp EM, Bierman PR, Caffee MW (2002) Using Be-10 and Al-26 to determine sediment generation rates and identify sediment source areas in an arid region drainage basin. *Geomorphology* 45(1-2):89–104.
35. Cockburn HAP, Brown RW, Summerfield MA, Seidl MA (2000) Quantifying passive margin denudation and landscape development using a combined fission-track thermochronology and cosmogenic isotope analysis approach. *Earth Planet Sci Lett* 179(3-4):429–435.
36. DiBiase RA, Whipple KX, Heimsath AM, Ouimet WB (2010) Landscape form and millennial erosion rates in the San Gabriel Mountains, CA. *Earth Planet Sci Lett* 289(1-2):134–144.
37. Duxbury J (2009) Erosion rates in and around Shenandoah National Park, VA, determined using analysis of cosmogenic Be-10. MSc Thesis (University of Vermont, Burlington, VT).

38. Granger DE, Riebe CS, Kirchner JW, Finkel RC (2001) Modulation of erosion on steep granitic slopes by boulder armoring, as revealed by cosmogenic Al-26 and Be-10. *Earth Planet Sci Lett* 186(2):269–281.
39. Heimsath AM, Chappell J, Dietrich WE, Nishiizumi K, Finkel RC (2000) Soil production on a retreating escarpment in southeastern Australia. *Geology* 28(9):787–790.
40. Heimsath AM, Chappell J, Dietrich WE, Nishiizumi K, Finkel RC (2001) Late Quaternary erosion in southeastern Australia: A field example using cosmogenic nuclides. *Quat Int* 83-5:169–185.
41. Heimsath AM, Dietrich WE, Nishiizumi K, Finkel RC (2001) Stochastic processes of soil production and transport: Erosion rates, topographic variation and cosmogenic nuclides in the Oregon Coast Range. *Earth Surf Process Landf* 26(5):531–552.
42. Heimsath AM, Chappell J, Finkel RC, Fifield K, Alimanovic A (2006) Escarpment erosion and landscape evolution in southeastern Australia. *Spec Pap 398: Tectonics, Climate, and Landscape Evolution*, eds Willett SD, Hovius N, Brandon MT, Fisher DM (Geol Soc of Am, Boulder, CO), pp 173–190.
43. Jakica S, et al. (2011) Geomorphic and cosmogenic nuclide constraints on escarpment evolution in an intraplate setting, Darling Escarpment, Western Australia. *Earth Surf Process Landf* 36(4):449–459.
44. Kirchner JW, et al. (2001) Mountain erosion over 10 yr, 10 k.y., and 10 m.y. time scales. *Geology* 29(7):591–594.
45. Lal D, et al. (2004) Erosion history of the Tibetan Plateau since the last interglacial: Constraints from the first studies of cosmogenic 10Be from Tibetan bedrock. *Earth Planet Sci Lett* 217(1-2):33–42.
46. Morel P, von Blanckenburg F, Schaller M, Kubik PW, Hinderer M (2003) Lithology, landscape dissection and glaciation controls on catchment erosion as determined by cosmogenic nuclides in river sediment (the Wutach Gorge, Black Forest). *Terra Nova* 15(6):398–404.
47. Nichols K, Bierman PR, Hooke RLB, Clapp EM, Caffee MW (2002) Quantifying sediment transport on desert piedmonts using Be-10 and Al-26. *Geomorphology* 45(1-2):105–125.
48. Nichols KK, et al. (2006) Dates and rates of arid region geomorphic processes. *GSA Today* 16(8):4–11.
49. Nichols KK, et al. (2007) Timing of surficial process changes down a Mojave Desert piedmont. *Quat Res* 68(1):151–161.
50. Ouimet WB, Whipple KX, Granger DE (2009) Beyond threshold hillslopes: Channel adjustment to base-level fall in tectonically active mountain ranges. *Geology* 37(7):579–582.
51. Palumbo L, Hetzel R, Tao M, Li X (2010) Catchment-wide denudation rates at the margin of NE Tibet from in situ-produced cosmogenic 10Be. *Terra Nova* 23(1):42–48.
52. Quigley MC, Sandiford M, Fifield K, Alimanovic A (2007) Bedrock erosion and relief production in the northern Flinders Ranges, Australia. *Earth Surf Process Landf* 32(6): 929–944.
53. Riebe CS, Kirchner JW, Granger DE, Finkel RC (2000) Erosional equilibrium and disequilibrium in the Sierra Nevada, inferred from cosmogenic Al-26 and Be-10 in alluvial sediment. *Geology* 28(9):803–806.
54. Riebe CS, Kirchner JW, Finkel RC (2003) Long-term rates of chemical weathering and physical erosion from cosmogenic nuclides and geochemical mass balance. *Geochim Cosmochim Acta* 67(22):4411–4427.
55. Riebe CS, Kirchner JW, Finkel RC (2004) Erosional and climatic effects on long-term chemical weathering rates in granitic landscapes spanning diverse climate regimes. *Earth Planet Sci Lett* 224(3-4):547–562.
56. Riebe CS, Kirchner JW, Finkel RC (2004) Sharp decrease in long-term chemical weathering rates along an altitudinal transect. *Earth Planet Sci Lett* 218(3-4): 421–434.
57. Schaller M, et al. (2002) A 30,000 yr record of erosion rates from cosmogenic Be-10 in Middle European river terraces. *Earth Planet Sci Lett* 204(1-2):307–320.
58. Small EE, Anderson RS, Hancock GS (1999) Estimates of the rate of regolith production using Be-10 and Al-26 from an alpine hillslope. *Geomorphology* 27(1-2):131–150.
59. Small EE, Anderson RS, Repka JL, Finkel RC (1997) Erosion rates of alpine bedrock summit surfaces deduced from in situ Be-10 and Al-26. *Earth Planet Sci Lett* 150(3-4): 413–425.
60. Stock GM, et al. (2009) Spatial and temporal variations in denudation of the Wasatch Mountains, Utah, USA. *Lithosphere* 1(1):34–40.
61. Weissel JK, Seidl MA (1998) *Rivers over Rock: Fluvial Processes in Bedrock Channels*, eds Tinkler K, Wohl EE (AGU, Washington, DC), Geophys Monogr Ser, Vol 107, pp 189–206.
62. Placzek CJ, Matmon A, Granger DE, Quade J, Niedermann S (2010) Evidence for active landscape evolution in the hyperarid Atacama from multiple terrestrial cosmogenic nuclides. *Earth Planet Sci Lett* 295(1-2):12–20.

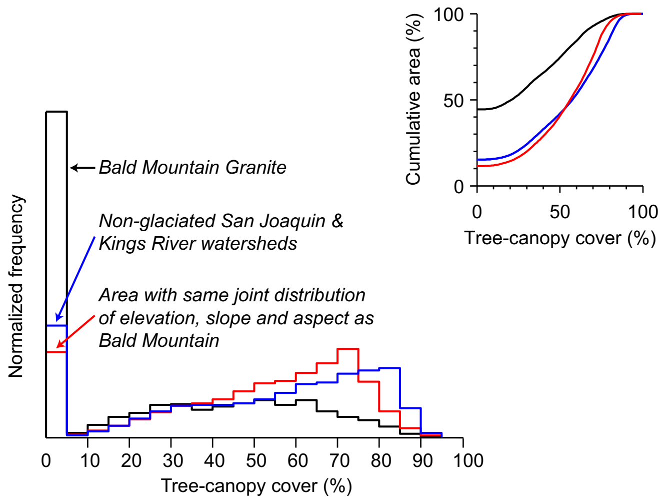

Fig. S1. Multivariate comparison of tree-canopy cover in area underlain by Bald Mountain Granite (see Fig. 1 for location) and surrounding nonglaciated landscape, shown as normalized histograms (*Bottom Left*) and cumulative density functions (*Upper Right*). Nearly 45% of the Bald Mountain Granite is devoid of tree-canopy cover (black line). In comparison, the surrounding 3,500 km^2 of nonglaciated terrain in the San Joaquin and Kings River watersheds has a significantly lower proportion of bare and sparsely vegetated area (blue line). The fraction of bare area is likewise lower for a subsampled 150 km^2 region that is identical to Bald Mountain in its multivariate probability distribution of slope, aspect, and elevation (red line). The offset between the black and red lines demonstrates that the paucity of vegetation on Bald Mountain cannot be explained by climatic or topographic factors. Rather it is consistent with lithologic control on vegetation across the site (as shown in Figs. 1–3 of the main article). Here, slope, aspect, and elevation are assumed to capture local differences in climate and topography. Our analysis was performed at the 30-m scale, which is the native resolution of the tree-canopy cover dataset (4). Aspect was derived from a 30-m DEM. We derived slope from a 10-m DEM and resampled the results into a 30-m–scale raster to match the other datasets. The multivariate probability distribution of slope, aspect, and elevation for all of the 30 m pixels in Bald Mountain was binned in three dimensions, and the surrounding landscape (i.e., the region outside of Bald Mountain) was randomly subsampled to replicate the 3D distribution of Bald Mountain data. To produce the plot shown, we split Bald Mountain into six elevation bins, three slope bins, and five aspect bins. Results are not strongly sensitive to bin size.

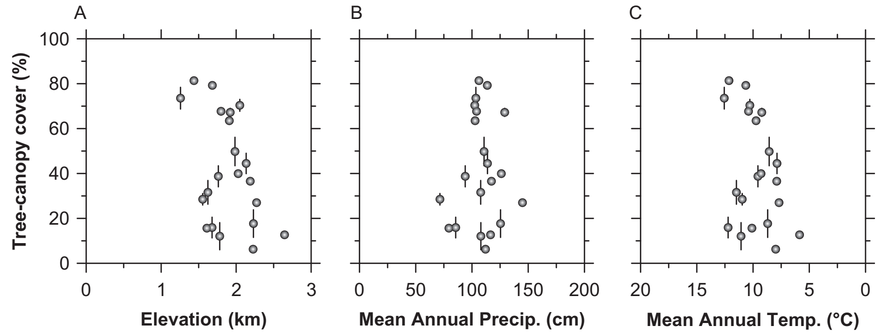

Fig. S2. Site-wide average (±SEM) tree-canopy versus site-wide averages of elevation (*A*), average annual precipitation (*B*), and mean annual temperature plotted backward to reflect increasing elevation (*C*). Neither elevation nor these average climate indices can explain the variations in forest cover across the sites. Figs. 1*B* and 3 (main text) show sample locations and Dataset S4 tabulates data.

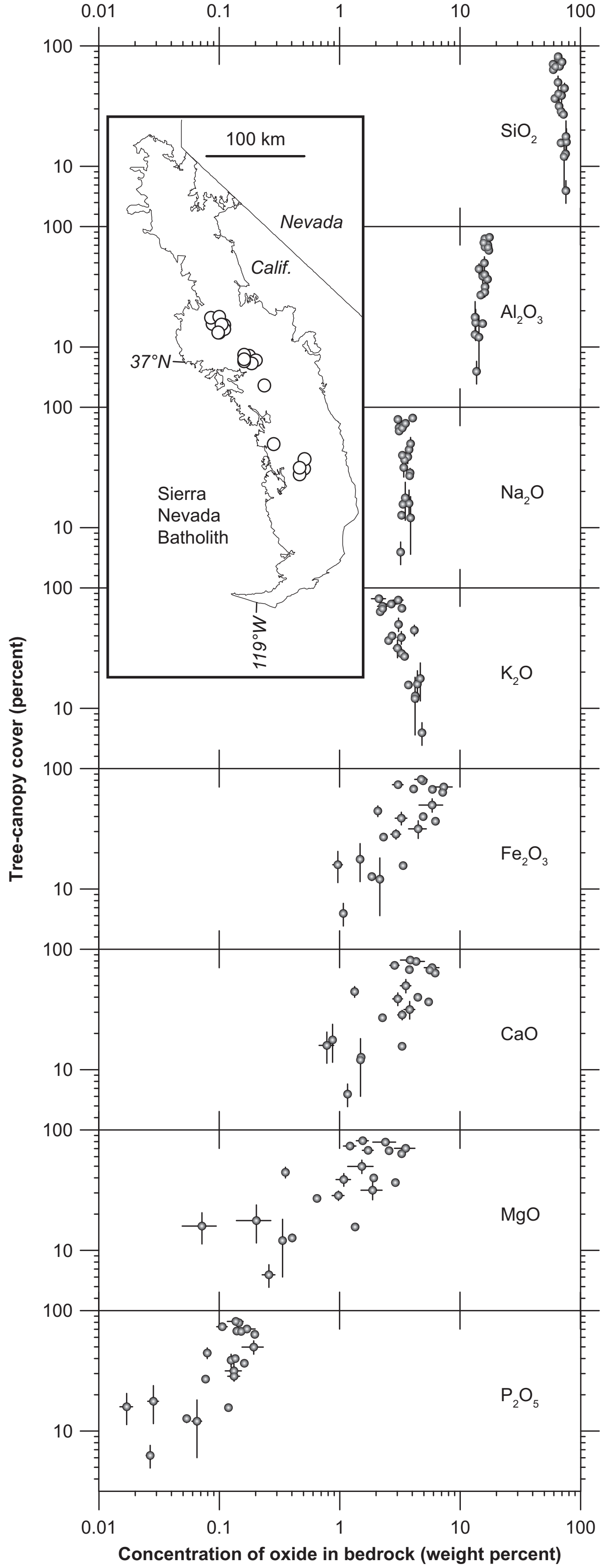

Fig. S3. Site-wide averages of tree-canopy cover versus site-wide average major and minor element concentrations from bulk geochemical analyses of bedrock samples. Error bars correspond to SEMs of data reported in Dataset S4. These plots show the same data as Fig. 3 (main text). Here they are logarithmically transformed to reveal relative differences in canopy cover and bedrock geochemistry. Tree-canopy cover spans more than an order of magnitude across the sites, comparable to the large relative differences in P, Mg, Ca, and Fe concentrations. Site locations are shown on map (*Inset*).

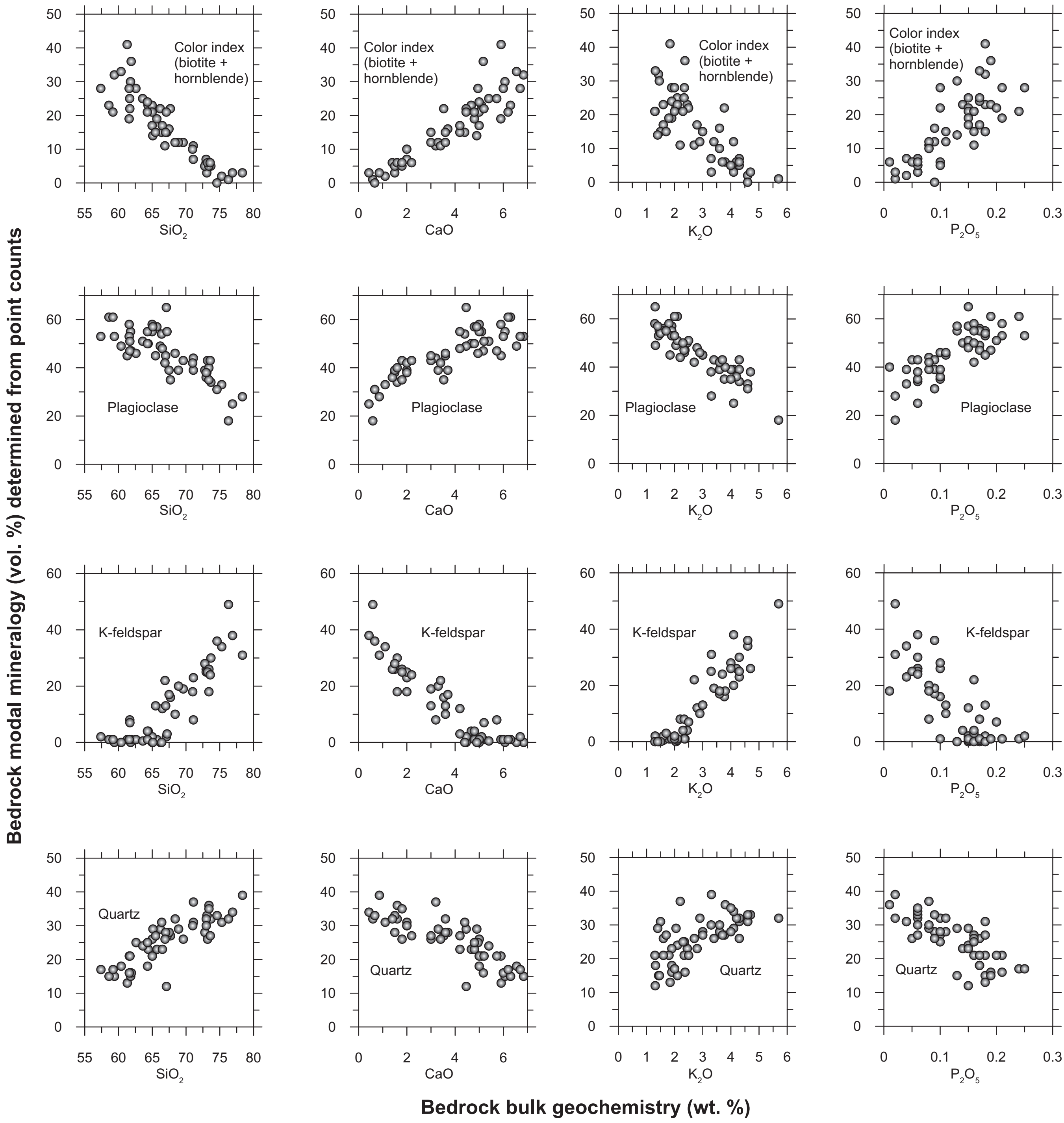

Fig. S4. Modal mineralogy covaries closely with bulk-elemental composition in bedrock samples from a subset of plutons considered in the main text. K-feldspar is nearly absent from rocks with low silica content, whereas the mafic minerals biotite and hornblende are nearly absent from rocks with high silica content. Data were originally reported in ref. 1 but are included for completeness in Dataset S5. When the trends in mineralogy and geochemistry shown here are coupled with trends in tree-canopy cover and geochemistry shown in Fig. 3 (main text), it is evident that tree-canopy cover generally increases with color index and plagioclase content and decreases with quartz and K-feldspar content in bedrock.

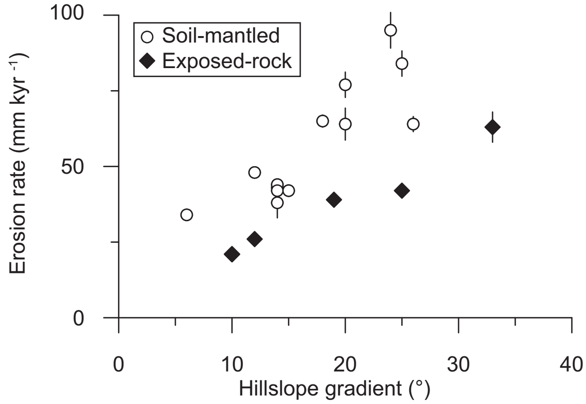

Fig. S5. Catchment-wide ^{10}Be-inferred erosion rates from the western Sierra Nevada increase with increasing average hillslope gradient (Dataset S6). Vertical error bars reflect propagated analytical uncertainties; note that some error bars are smaller than the symbol size. For a given average hillslope gradient, predominantly soil-mantled catchments (open circles, $n = 13$) have a higher erosion rate than predominantly exposed-rock catchments (black diamonds, $n = 7$). We calculated centered, least-squares regression statistics for the relationship between erosion rate and hillslope gradient for each surface-cover class. We found that the erosion-rate intercept (which represents the erosion rate predicted at the overall average hillslope gradient of 17°) is significantly higher ($P < 0.05$) for soil-mantled catchments (56.6 ± 3.0 mm kyr^{-1}) than for exposed-rock catchments (33.3 ± 1.1 mm kyr^{-1}). Note these averages differ from the averages in Fig. 4 of the main text because they only pertain to the catchment-scale estimates of erosion rates.

Other Supporting Information Files

Datasets S1–S7 (XLS)